Fast Two-step Blind Optical Aberration Correction

Thomas Eboli, Jean-Michel Morel, Gabriele Facciolo

Fast Two-step Blind Optical Aberration Correction

Thomas Eboli, Jean-Michel Morel, and Gabriele Facciolo

Université Paris-Saclay, ENS Paris-Saclay, CNRS, Centre Borelli, France
https://github.com/teboli/fast_two_stage_psf_correction

Abstract. The optics of any camera degrades the sharpness of photographs, which is a key visual quality criterion. This degradation is characterized by the point-spread function (PSF), which depends on the wavelengths of light and is variable across the imaging field. In this paper, we propose a two-step scheme to correct optical aberrations in a single raw or JPEG image, *i.e.,* without any prior information on the camera or lens. First, we estimate local Gaussian blur kernels for overlapping patches and sharpen them with a non-blind deblurring technique. Based on the measurements of the PSFs of dozens of lenses, these blur kernels are modeled as RGB Gaussians defined by seven parameters. Second, we remove the remaining lateral chromatic aberrations (not contemplated in the first step) with a convolutional neural network, trained to minimize the red/green and blue/green residual images. Experiments on both synthetic and real images show that the combination of these two stages yields a fast state-of-the-art blind optical aberration compensation technique that competes with commercial non-blind algorithms.

Keywords: Point-spread function, optical aberrations, blind deblurring, spatial Gaussian filter, edge non-linear filtering.

1 Introduction

Sharpness is a critical criterion for both photographers and scientific applications. In the absence of motion and with perfect focus, there will always be blur in the raw photographs, caused by the optics. The choice of the objective is thus important to take the best possible images and its quality is often characterized by its point spread function (or *PSF*), which is the combination of the optical aberrations transforming a white point in the ideal focal image into a colored spot. In real images, the PSF introduces optical aberrations degrading the global sharpness and introducing colored fringes next to the contrasted edges, see for instance in Fig. 1 for a mid-entry camera/lens pair.

Since most cameras use glass or plastic lenses, the effects of the PSF cannot be avoided but only compensated by either switching to a better objective with a smaller colored spot, or post-processing the aberrated photographs. The first solution seems to be the most appealing since it solves the problem at its root but the top-of-the-line objectives are too expensive for most consumers.

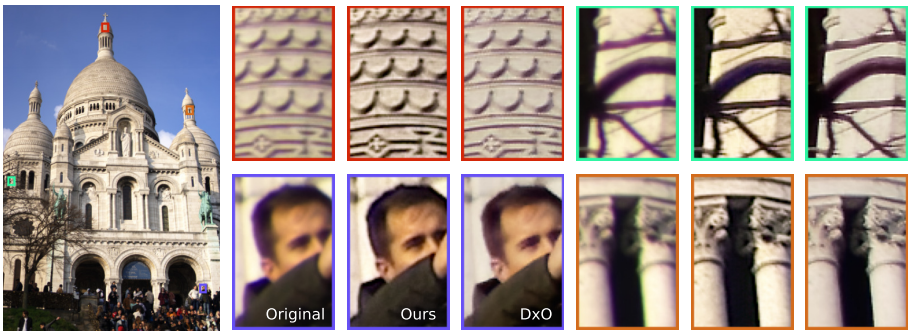

Fig. 1: We propose a blind method to correct the optical aberrations caused by the point-spread function of the lens, without any prior on the lens or the camera to restore the image. We sharpen and compensate the visible colored fringes in a 24 megapixels (4000×6000) photograph taken with a Sony α6000 camera and a Sony FE 35mm $f/1.8$ lens at maximal aperture in 2 seconds on a NVIDIA 3090 GPU, achieving a visual result comparable to that of the non-blind algorithm of DxO PhotoLab (best seen on a computer screen).

Furthermore, most pictures are taken nowadays with smartphone cameras that have low-quality and non-interchangeable lenses, hence the relevance of efficient algorithmic solutions. Optical aberration correction, along with denoising, demosaicking and distortion and vignetting correction, is among the earliest processing steps of any commercial editing software, *e.g.,* Adobe Lightroom or DxO PhotoLab. Figure 2 shows an example of such an image processing pipeline. However, these software rely on accurate calibration of camera/objective pairs, which are based on exhaustive measurements of all the possible camera settings.

In this paper, we propose a blind optical aberration compensation technique that can be applied to any raw or JPEG image *without* any prior knowledge of the camera or lens. Unlike the current state of the art that casts this problem correction as an instance of blind deblurring with RGB kernels [23, 24, 32], we follow [18] and decompose optical aberration compensation into a two-stage scheme that first removes lens blur and second compensates the remaining color fringes. We show a visual comparison with the non-blind commercial solution of DxO in Figure 1. Our deblurring stage relies on the observation that the real RGB PSF measurements of [3] and the parametric kernels of [19] (which model local RGB kernels of real data), fit 2D Gaussian filters defined by just seven parameters. We confirm that these Gaussian filters verify the "mild blur" condition needed to apply the fast blind deblurring algorithm proposed in [8]. We thus adapt this approach to our problem to increase the sharpness of overlapping patches, assuming the blur is uniform on their supports. We correct the remaining effects due to the color-dependent warp by independently processing the red and blue channels using a small convolutional neural network (CNN) trained to minimize the red/green and blue/green image residuals. This is motivated by

the analysis of color fringes in [7] showing that the profile of this image transformation is directly related to the intensity of the colored fringes. Thanks to the above decomposition, a shallow 160K-parameter CNN is enough to achieve state-of-the-art results. We finally gather the patches processed by the CNN.

Our approach presents several advantages over concurrent academic works and commercial solutions. First, the blind deblurring stage is very fast and memory-efficient since it leverages the Gaussian model of [19] and the approximated deconvolution scheme from [8]. Moreover, since our 2D Gaussian lens blur approximation only has a seven parameters, it is easy to compute. Yet, the method yields satisfactory visual results. Second, our approach does not suppose any parametric warp model to represent the displacements of the edges in the red and blue channels, which results in a more accurate prediction and in a method that may run either on crops or the full image. Furthermore, since the colored fringes are relatively thin, a small, fast and memory-efficient CNN architecture yields satisfactory results. Third, since the method is blind to the camera and lens settings, we restore any photograph without prior calibration with a target.

The contributions of this paper are summarized as follows:

- We decompose the optical aberration into blur and warp components and in particular, characterize the blur with local 2D Gaussian kernels with seven parameters. We validate this model with the PSFs measurements of [3];
- we sequentially compensate the blur and the warp. We apply the blind deblurring algorithm of [8] to sharpen the image, showcasing its effectiveness for optical aberration correction, and then remove the remaining color fringes with a novel 2-channel CNN trained to minimize the image residual between the red/blue and green channels;
- quantitative experiments on both synthetic and real images show that our method accurately compensates both the blur and the colored edges misalignments caused by the PSF. In particular it is 20 times faster and has 100 times less parameters than the current state of the art; and
- we show that our blind approach generalizes to real images even competing with commercial image editing software running in a non-blind setting. Our method processes a 12 megapixels image in 1 second on a GPU with a non-optimized code.

2 Related work

Knowing the PSF associated to an image or a lens may be useful for two tasks: accurately evaluating the lens quality and removing the lens blur with a non-blind deblurring algorithm. The PSF may be estimated from a single photograph of a calibration target or from natural images. Trimeche *et al.* [30] and Joshi *et al.* [17] take raw photographs of targets with contrasted edges, *e.g.,* a checkerboard, and solve an optimization problem to predict a grayscale local filter. The same idea is proposed by Brauers *et al.* [5], Delbracio *et al.* [9] and Heide *et al.* [15] who use carefully designed noise patterns to facilitate the optimization

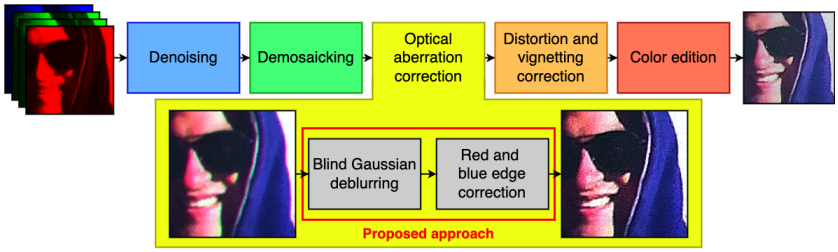

Fig. 2: Main stages of an editing software, processing a raw photograph into a JPEG image. We focus on the optical aberration correction module, usually just after denoising and demosaicking and before further color and geometry corrections. We decompose this block into two stages: (i) we improve sharpness with a blind deblurring algorithm, and (ii) we align the contrasted red and blue edges to remove the colored fringes at the vicinity of contrasted edges.

and achieve sub-pixel grayscale filters estimation. Instead of using edge and noise patterns, Schuler *et al.* [24] and Bauer *et al.* [3] take photographs of LED panels, which allow them to directly observe the local PSFs without any optimization, simply by recording how the white LED dots become colored spots in the images.

All these techniques may predict accurate estimates of the PSF but are only valid for specific lens settings and for a sparse set of locations in the image, making them unsuitable at non-measured pixel locations or lens settings. A few approaches intend to fill this void: Kee *et al.* [19] and Shih *et al.* [26] interpolate the PSF for various focal length/aperture aperture pairs by fitting a spatial Gaussian model and Hirsch and Schölkopf [16] predict RGB filters at unknown locations on the field of view with a kernel method.

However, if the goal is enhancing the image sharpness, blind kernel estimates designed to achieve the best deblurring, *i.e.,* without being faithful representations of the true local blurs, may suffice. For instance Joshi *et al.* [17] propose a variant of their target-based approach by assuming the latent sharp image has ideal step edges. Schuler *et al.* [25] predict a set of RGB linear filters covering the image, hypothesizing symmetries of the PSF, which is most of the time an inaccurate oversimplification for real lenses [10], and Yue *et al.* [32] and Sun *et al.* [27] additionally posit sharpness of the green channel, which is also an aggressive approximation when looking at real lens measurements [3]. Heide *et al.* [15] adopt instead a prior on the color and the location of edges across the color channels. After PSF estimation, correction boils down to non-blind deblurring by solving an inverse problem [20], or learned with a CNN [23]. In this paper, we adopt a 2D Gaussian model to approximate the local blur caused by the PSF, which is validated by observations of [19] and that can be efficiently estimated from a single image [8]. Furthermore, [8] shows that no prior is needed to achieve satisfactory deblurring results with these simple kernels.

Blur is only one facet of a PSF, which also warps the color planes of a photograph, resulting in color fringes next to the edges. Boult and Wolberg [4]

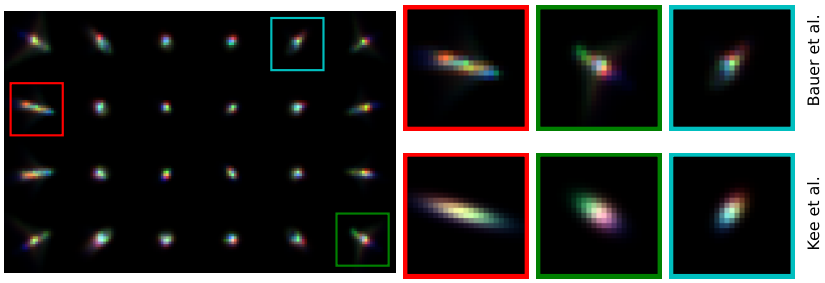

Fig. 3: A 4×6 subset of the Canon EF 16-35mm f/2.8L II USM PS lens PSF measurement of Bauer *et al.* [3] at maximal aperture and shortest focal length, a panel of three zoomed local kernels and the Gaussian approximations of Kee *et al.* [19]. The spots, despite being non-parametric functions of the field of view, may be reasonably approximated with spatial Gaussian filters.

and Kang [18] align the red and blue channels with the green one by means of a radial warp model. Chang *et al.* [7] do not suppose any model on the warp and instead remove the fringes with a linear filter applied in the neighborhood if the most salient edges, in the red/green and blur/green image residuals. These image residuals contain all the information to characterize these colored artifacts and are used in the present work to train a CNN, a non-linear variant of [7].

3 Local PSF parametric model

3.1 Optical aberrations model

In the absence of diffraction, which is a realistic assumption for usual aperture sizes, typically below $f/11$, the PSF is the combination of the optical aberrations. The Seidel theory [28] decomposes them into five monochromatic aberrations: spherical, coma, astigmatism, field curvature and geometric distortion, and two chromatic aberrations: lateral and longitudinal.

The combination of the first four monochromatic and the longitudinal aberrations boils down to converting a point in the ideally focused image into a spot whose size depends on the wavelength and its position on the focal plane [18]. Geometric distortion bends parallel lines and necessitates two or more images to calibrate the camera [33], and is thus not addressed in this presentation. However, lateral aberrations are also geometric transformations, but which warp differently each color component of an edge, leading to visible colored fringes [7]. Figure 3 illustrates a PSF measurement of a real lens obtained by Bauer *et al.* [3].

Kang [18] already proposed a forward model for optical aberrations with simultaneous blur and color warp. Chang *et al.* [7] set an order, that we follow in this paper, by running a sharpening stage prior to edge correction. From the

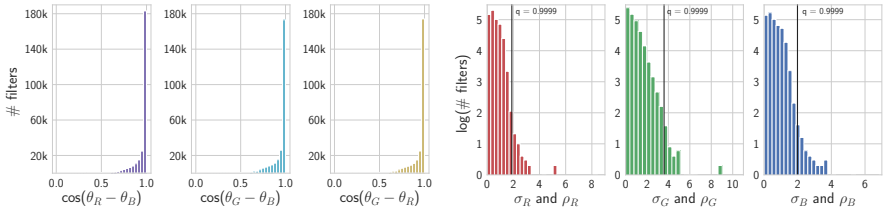

(a) Assumption on θ_c. (b) Assumption on σ_c and ρ_c.

Fig. 4: Experimental validation of the assumptions on the parameter triplets $(\theta_c, \sigma_c, \rho_c)$. Left: We measure the similarity θ_R, θ_G and θ_B and show the strong correlation across the color channel directions. Right: We compute the histogram of σ_c and ρ_c $(c = R, G, B)$ and its 0.9999-th quantile, and show that almost all standard deviation values are under 4.

above analysis, and considering also degradation caused by the sensor, (mosaicking, noise and saturation), we derive the following raw image formation model for a single color channel $c = (R, G, B)$:

$$r_c = s \circ m_c \left(g_c \circ w_c(u_c) + \varepsilon \right) \quad \text{with} \quad \varepsilon \sim \mathcal{N}(0, \alpha g_c \circ w_c(u_c) + \beta), \tag{1}$$

where u_c and r_c are the sharp and raw color planes, w_c is the inter-color warp caused by lateral chromatic aberrations (recall that we neglect geometric distortion in this presentation), g_c is the spatially-varying blur caused by the remaining aberrations, $\circ$ is the composition operator, m_c is the decimation caused by the mosaicking filter, s is the sensor saturation and ε is the image noise modeled with the heteroscedastic normal model of [12], parameterized with shot and read noise weights α and β. We call v the denoised and demosaicked version of the raw image r, which should therefore be close to the RGB aberrated image *before* mosaicking and degradation with noise.

3.2 Blur parametric approximation

An image of the local blur may be obtained with photographs of a known reference like a target [9,17,30]. It gives an accurate estimate of the blur but only in a controlled environment with special gear. We instead follow Kee *et al.* [19] and approximate the local blur g_c in a color channel $(c = R, G, B)$ with a zero-mean 2D Gaussian filter. Blur estimation thus boils down to a direct blind estimation of few parameters from any photograph.

Parametric monochromatic aberrations. A zero-mean 2D Gaussian is fully characterized by three parameters: the angle of the principal direction θ and the standard deviation values σ in θ and ρ in the direction $\theta + \pi/2$:

$$k(x) = [2\pi \det(\Sigma)]^{-\frac{1}{2}} \exp\left(-\frac{1}{2} x^\top \Sigma^{-1} x \right), \tag{2}$$

for the locations x in the support of k and with a covariance matrix Σ:

$$\Sigma = R(\theta)^\top \begin{bmatrix} \sigma^2 & 0 \\ 0 & \rho^2 \end{bmatrix} R(\theta), \tag{3}$$

where $R(\theta)$ is the 2D rotation matrix of angle θ.

Parametric longitudinal chromatic aberrations. Incorporating the contribution of longitudinal chromatic aberrations yields a kernel k_c, or equivalently a triplet $(\theta_c, \sigma_c, \rho_c)$, for each color $c = (R, G, B)$. Thus, our RGB parametric local blur model has nine parameters.

Bounding the parameters with real data. We use the real PSF measurements by Bauer *et al.* [3] and the non-blind Gaussian approximation technique of Kee *et al.* [19], both shown in Figure 3, to reduce the set of parameters. Bauer *et al.* took photographs with 70 lens settings of a 52×78-point LED array, which yields about 280,000 local RGB PSF measurements (g_R, g_G, g_B). Since the aperture is kept between $f/1.4$ and $f/5.6$, the contribution of diffraction to the local spot is negligible.

Following Kee *et al.*, we compute the covariance matrices of the kernels k_c that best fit the measurements g_c $(c = R, G, B)$, and whose eigendecomposition return the triplets $(\theta_c, \sigma_c, \rho_c)$. From this large corpus of triplets, we draw two conclusions: (i) the direction θ_c is roughly the same for each color c, and (ii) the standard deviation values σ_c and ρ_c are contained in the segment $[0.2, 4]$. The first observation limits the actual number of parameters to be estimated to only seven, the information on the principal direction being contained in a single scalar θ, whereas the second observation ensures that we can use the fast blind deblurring technique of [8] to predict k_c.

We experimentally validate these claims by first computing the cosine similarity of the pairs of eigenvectors directed by θ_c of the approximate filters k_c $(c = R, G, B)$. We show in Figure 4 (a) that these vectors are always aligned, confirming our first observation. Second, we plot in Figure 4 (b) the cumulative distribution function of the standard deviation values σ_c and ρ_c and show that only a negligible amount of candidates are above 4. We also see that a realistic floor value is at 0.2, thus suggesting the standard deviations for modeling realistic parametric lens blurs are within a segment $[0.2, 4]$, validating our second claim. In conclusion, we can reasonably adapt the blind deblurring technique of Delbracio *et al.* [8] to estimate a local PSF blur with only seven blur parameters.

4 Proposed method

We decompose the image into patches, *e.g.,* with 25% or 50% overlap, in which we assume that the blur is uniform, and we remove the local PSF in two steps. We first remove the local uniform blur with the blind Gaussian deblurring technique of [8]. Second, we eliminate the colored artifacts caused by the warp next the salient deblurred edges using a CNN, which is inspired on the method [7]. The selected deblurring and colored artifact correction methods strike a good compromise between speed and accuracy. Other combinations of methods were

Algorithm 1: Proposed PSF removal method

Data: Aberrated v, coefficients (C, σ_b), estimator ϕ_ν
Result: Aberration-free $\widehat{u}$
Compute blur direction θ from v_G with Eq. (4);
Compute blur standard deviations σ_c and ρ_c $(c = R, G, B)$ with Eq. (5);
Compute approximate filter k_c $(c = R, G, B)$ with Eqs. (2) and (3);
Compute approximate inverse filter $p(k_c) = -3(k_c * k_c) - k_c + 3\delta$ $(c = R, G, B)$;
Compute deblurred image z_c $(c = R, G, B)$ with Eq. (6);
Compute aligned channel $\widehat{u}_c$ $(c = R, B)$ with Eq. (7);
Build $\widehat{u} = [\widehat{u}_R, z_G, \widehat{u}_B]$;

also considered leading to worse results or much slower methods, we refer to the supplementary material for details.

Algorithm 1 summarizes our approach for restoring a single patch. After all the patches are deblurred and processed by the CNN, we put them back to their initial locations in the image using a Hamming window to limit fusion artifacts.

4.1 Blind Gaussian deblurring

As explained above, the combination of the monochromatic and longitudinal aberrations is a spatially-varying blur. We split the image into overlapping patches where the local blur is supposed uniform, and predict a zero-mean Gaussian kernel for which we approximate a deconvolution filter, adapting the procedure of [8]. In brief, this technique quickly estimates the parameters (ρ, σ, θ) from a blurry grayscale image, and run an approximate inverse filter for the corresponding 2D Gaussian kernel. It is particularly effective for "mild" blurs that may be captured by Gaussian kernels with standard deviation under 4.

This blind deblurring technique is valid in our context since PSFs are mostly small blurs according to the previous section and previous art [3, 19, 24]. The authors of [8] thus demonstrate that their approach achieves similar result to that of CNNs, but for a fraction of the speed and memory. We show in this work it is well suited for lens blur removal. Since, according to our analysis, the blur orientation is the same for all color channels we find θ by arbitrarily computing the infinite norm of the directional derivative of the green channel and picking the direction with the smallest value, *i.e.,* where the blur is the strongest:

$$\theta = \underset{\varphi}{\operatorname{argmin}} \, \|\nabla_\varphi n(v_G)\|_\infty, \tag{4}$$

where $\nabla_\varphi v = \cos(\varphi)\nabla_x v + \sin(\varphi)\nabla_y v$, ∇_x and ∇_y are the horizontal and vertical derivative operators, and n is a normalization function detailed in [8] and in the supplemental material. For the range of standard deviation values we are interested with, Delbracio *et al.* [8] empirically show that there exists an affine relationship between the variance of a Gaussian blur and the infinite norm of the image gradients in its principal directions θ and $\theta + \pi/2$. Let C be the slope

and σ_b be the intercept of this model. The empirical affine model reads

$$\sigma_c = \sqrt{\frac{C^2}{\|\nabla_\theta n(v_c)\|_\infty^2} - \sigma_b^2} \text{ and } \rho_c = \sqrt{\frac{C^2}{\|\nabla_{\theta+\frac{\pi}{2}} n(v_c)\|_\infty^2} - \sigma_b^2}, \tag{5}$$

where $c \in \{R, G, B\}$ and θ is the direction previously computed. The hyperparameters are tuned with the protocol of [8]. Minimizing with the linear programming algorithm the sum of ℓ_1 differences between the norm of the gradient and the variance for 600 synthetic blurry images and known corresponding Gaussian filters yields $C = 0.415$ and $\sigma_b = 0.358$ for demosaicked images before gamma correction, and $C = 0.371$ and $\sigma_b = 0.453$ for JPEG images.

The resulting triplet $(\theta, \sigma_c, \rho_c)$ is used to build the covariance matrix defined in Eq. (3) and thus the 2D Gaussian kernel k_c ($c = R, G, B$). As in [8], we carry out non-blind deblurring by computing the approximate inverse filter $p(k) = -3(k*k) - 4k + 3\delta$ (δ denotes the Dirac filter), and deconvolve each color channel c ($c = R, G, B$) with:

$$z_c = p(k_c) * v_c. \tag{6}$$

We have also tried an inverse filter obtained with Fourier transform, *e.g.,* [11], but noticed that the filter $p(k_c)$ ($c = R, G, B$) achieves better results in our experiments. Each $h \times w$ image z_c is a sharp version of v_c, however due to lateral chromatic aberration, the red and blue channels still have shifted edges compared to their counterparts in the aberration-free image u, which results in artifacts in the vicinity of contrasted and sharp edges.

4.2 Red and blue edge correction

Lateral chromatic aberrations introduce a shift between the color channels. Usual techniques for removing these colored artifacts use parametric red-to-green and blue-to-green warp models, for instance taking the form of a global radial transformation [4,18] or local translations [25,32]. In this context registration is hard since different color channels may have different edge profiles and in these contrasted areas demosaicking may produce incorrect color predictions, preventing perfect edge alignment and resulting in residual edge artifacts. Modeling the warp thus seems to be a harder problem than the original one. Conversely, we follow Chang *et al.* [7] remkarking that lateral aberrations result in color fringes next to the most salient edges; Filtering the edges, without any explicit model on the warp or information on the edge location, is enough for effective correction. In this work we propose a residual CNN, that takes as input z_G and z_R or z_B and returns an image $\widehat{u}_R$ or $\widehat{u}_B$ whose edges should be aligned with those of z_G. If we call this CNN ϕ with parameter ν, our approach reads for $c = R, B$:

$$\widehat{u}_c = z_c - \phi_\nu(z_c, z_G). \tag{7}$$

We then combine $\widehat{u}_R$, z_G and $\widehat{u}_B$ into a single restored image. The network ϕ_ν is a UNet with four convolutional layers of respectively 16, 32, 64 and 64 feature

maps in the encoder part and a mirrored structure in the decoder, each followed by batch normalization and ReLU activation.

Training of ϕ. For estimating the network parameters ν, we use synthetic supervisory data. We follow Brooks *et al.* [6] to convert 128×128 JPEG patches into linear RGB ones, just after demosaicking, but without noise or aberrations. We then apply the forward model (1) to generate their aberrated and mosaicked raw counterparts. We sample orientations in $[0, \pi)$, and standard deviations in $[0.2, 4]$ to build an RGB Gaussian kernel to blur a given "unprocessed" training image u from the DIV2K dataset. Then translate the red and blue channels with sub-pixel shifts sampled in $[-4, 4]^2$ to model the local lateral chromatic aberration, add Poissonian-Gaussian noise, mosaick with the Bayer filter and clip its pixel values between 0 and 1, ultimately resulting in a raw image r. The translation value range is empirically set after having observed photographs taken with a couple of different lenses. Nonetheless, this arbitrary value leads to satisfactory restoration results in real images. To simulate the modules preceding the optical aberration brick in any image processing pipeline (see Fig. 1), we denoise and demosaick r respectively with the bilateral filter [29] and demosaicnet [13] to predict an aberrated RGB image v. We deblur v by removing the blur with Eqs. (4) to (6) to predict a sharp version z with aberrated edges.

As demonstrated by Chang *et al.* [7], the chroma images $z_R - z_G$ and $z_B - z_G$ isolate the lateral chromatic aberrations and are sufficient to remove the colored artifacts. Thus, instead of training our model to minimize a loss of the sort $\|\widehat{u} - u\|_1$ as usual, we force ϕ to minimize these quantities for N synthetic image pairs $(u^{(i)}, v^{(i)})$ with the training loss

$$\sum_{i=1}^{N} \sum_{c \in \{R,B\}} \left\| \left(u_c^{(i)} - u_G^{(i)} \right) - \left(z_c^{(i)} - \phi_\nu(z_c^{(i)}, z_G^{(i)}) - z_G^{(i)} \right) \right\|_1 , \tag{8}$$

where $z_c^{(i)} = p(k_c) * v_c^{(i)}$ $(c = R, G, B)$. Since the roles of the red and blue channels are symmetric, we have $2N$ supervisions from N pairs $(u^{(i)}, v^{(i)})$ $(i = 1, \ldots, N)$. We minimize Eq. (8) with the Adam optimizer whose initial learning rate is set to 3×10^{-4} and is multiplied by 0.5 when the validation loss plateaus for 10 epochs and with batch size set to 40.

5 Experiments

5.1 Blind grayscale PSF removal

We first measure the ability of the parametric estimation technique to help deblurring a real-world non-parametric PSF for a single color channel (the impact of lateral chromatic aberrations is kept for later in this presentation). We compute blur estimates with a panel of blur estimation techniques including ours, and quantitatively evaluate their impact on deblurring.

We convolve grayscale images u with the green components g_G of the local PSFs of Bauer *et al.* [3] to generate blurry images v, from which we predict a

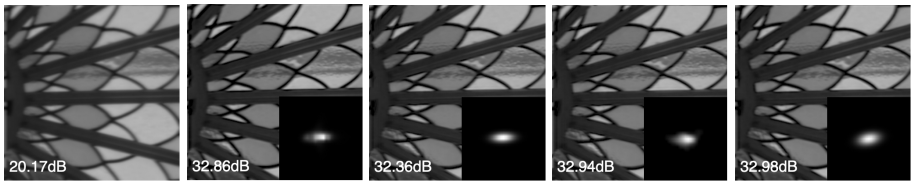

(a) Blurry. (b) GT's kernel. (c) [19]'s kernel. (d) [1]'s kernel. (e) Our's kernel.

Fig. 5: Qualitative result for blind deblurring with different kernel estimators. From left to right: The synthetic blurry image, the version deblurred with the ground truth kernel from [3], the oracle Gaussian approximation [19], the parametric kernel from [1] and our estimate. We use the polynomial p previously defined to achieve non-blind deblurring. All the techniques, except that of Kee *et al.* [19] achieve similar results but ours is blind and fast.

blur kernel $\widehat{g_G}$ with various kernel estimation techniques. We then compute a deconvolution filter $p(\widehat{g_G})$ and estimate a deblurred version $p(g_G) * v$ for each kernel estimation method in our panel composed of the non-blind parametric model of Kee *et al.* [19] and the blind non-parametric algorithm of Anger *et al.* [1]. We quantitatively compare the performance of the blur estimators with the SSIM ratio of Kee *et al.* comparing the relative quality of the image deblurred with the ground-truth kernel g_G over that restored with $\widehat{g_G}$:

$$R(\widehat{g_G}, g_G) = \frac{\text{SSIM}[p(g_G) * v, u] + 2}{\text{SSIM}[p(\widehat{g_G}) * v, u] + 2}. \tag{9}$$

Since the kernels of Bauer *et al.* may not be centered in zero, we adopt the ground-truth shifting strategy of Levin *et al.* [22] and crop the 15 pixel on the borders to compute $\text{SSIM}[p(g_G) * v, u]$. Figure 6 (a) shows the plots of the ratios R for the different kernel estimators on 870 synthetic images of size 400×400. The non-blind parametric technique of Kee *et al.* is an upper-bound to ours and logically achieves the best result, nonetheless we are just under it with a marginal gap, and in a blind fashion. We also exceed the performance of the non-parametric algorithm of Anger *et al.*, validating our blind Gaussian model for PSF removal. Figure 5 shows a deblurring example for different kernel estimates.

5.2 Lateral chromatic aberration compensation

We now validate the CNN ϕ to correct the lateral chromatic aberrations. However, to our knowledge, there is no benchmark or quantitative metric for this specific task. As a result, we have found that computing the norm of the image prior of Heide *et al.* [15] favoring aberration-free solutions, was the most relevant existing metric for this evaluation. Given an image z, we predict the red and blur corrected planes $\widehat{u}_R$ and $\widehat{u}_B$, compute their horizontal and vertical

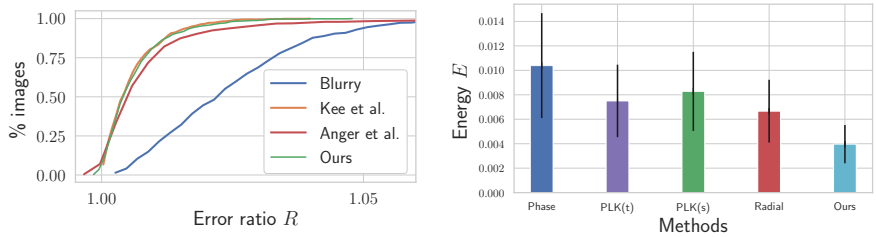

(a) Blind deblurring. (b) Edge correction.

Fig. 6: Quantitative analysis of the blind deblurring and the edge corrections modules with the metrics R and E of Eqs (9) and (10). Left: Comparison of the SSIM ratios R in Eq. (9) for kernels estimated as by Kee *et al.* [19], Anger *et al.* [1] and with our approach (the more on the left, the better). Our blind method competes with the non-blind technique of Kee *et al.* Right: Comparison of the energy E in Eq. (10) from Heide *et al.* [15] for edge corrections estimated by phase correlation [21], the pyramid Lucas-Kanade (PLK) algorithm of [2] predicting translations and similarities (PLK(t) and PLK(s)), the radial model of [18] and our CNN. Our approach achieves the best quantitative result.

gradients with ∇_x and ∇_y, and evaluate the following energy:

$$E(\widehat{u}_R, \widehat{u}_B, z_G) = \sum_{c=R,B} \sum_{j=x,y} \|(\nabla_j z_G)/z_G - (\nabla_j \widehat{u}_c)/\widehat{u}_c\|_1, \tag{10}$$

where the division is pixelwise. It may be seen as normalized variants of the color residuals of Chang *et al.* [7]. Note that this quantitative score does not necessitate a clean ground-truth, and thus can be used on real images. We thus take ten 24 megapixels photographs, of various environments (shown in the supplemental material), that are denoised and demosaicked with DxO PhotoLab 5, deblurred with our blind technique, and decomposed into 400×400 non-overlapping patches, resulting in 1,500 test images.

Figure 6 (b) compares the performance of our method with a classical radial model [18], and local parametric warps modeled with translations predicted with the phase correlation [21] or the pyramid Lucas-Kanade (PLK) [2] algorithms, or similarities also predicted with PLK. Our model achieves the best performance of the panel since it is trained to compensate the colored residuals. Note that phase correlation performs the worst among the considered methods, probably because the real blurs can affect differently the phase of different bands. The under-constrained PLK (similarity) method produces slightly worse results than the radial and PLK (translation) methods. A visual inspection of the restored images (reported in the supplementary material) confirms this quantitative analysis.

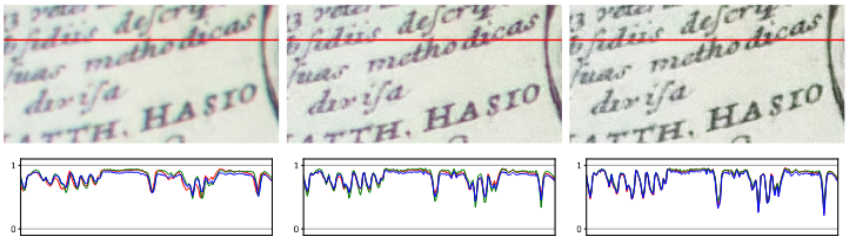

Fig. 7: Comparison of lateral chromatic aberration removal from a real raw image. From left to right: The blurry image, the version predicted by ϕ trained with the typical loss $\|\widehat{u} - u\|_1$ and the estimate from the one trained with the loss $\|(\widehat{u} - \widehat{u}_G) - (u - u_G)\|_1$. The model trained with the usual regression loss retains purplish edges whereas the variant gets rid of most of the aberrations.

5.3 Real-world examples

We test our method on real raw images and some datasets for existing images comparing our results with those of DxO PhotoLab 5. Figure 1 shows a real 24 megapixels photograph taken with a Sony α6000 camera and a Sony FE 35mm $f/1.8$ lens set at maximal aperture to maximize the chromatic aberration. The raw image is denoised and demosaicked with DxO PhotoLab prior to optical aberration compensation. We show in the supplemental material additional qualitative results for different lenses.

Computational efficiency. We evaluate the speed of the state-of-the-art CNN from [23] and our technique to process a 24 megapixel (6000×4000) photograph on a NVIDIA 3090 GPU. Our technique takes in average 1.7 seconds whereas that of [23] takes about 30 seconds on the same device. This is explained by the fact that our network only has 160K parameters for 33.1 gigaflops, whereas its counterpart counts 17 million parameters for 27.3 teraflops.

Impact of the training loss. We train ϕ_ν with a loss minimizing the red-green and blue-green residuals in the target u and prediction $\widehat{u}$ of the form $\|(\widehat{u} - \widehat{u}_G) - (u - u_G)\|_1$, which differs from the typical regression loss $\|\widehat{u} - u\|_1$. We show in Figure 7 the advantage of the loss (8) leveraging the observations of Chang *et al.* on chromatic aberrations. The model trained with the typical regression loss leads to purplish edges next to the contrasted edges, *i.e.,* the edges across the three color channels have been aligned but the intensities of the red and blue ones do not match that of the green channel, whereas the one trained with Eq. (8) predicts an image without any color artifact.

Restoring JPEG images. We have assumed so far that the raw image is available. However, we show that our blind method may also be applied to JPEG images when only this one is available. Figure 8 shows a restoration example from two images of [19] and [15] with the techniques of [23,32] and ours with the blur estimation coefficients (C, σ_b) calibrated for JPEG images (see Section 4.1). Our method, despite being blind, achieves the best visual result, predicting correct

(a) Blurry. (b) Yue *et al.* [32]. (c) Li *et al.* [23]. (d) Ours.

Fig. 8: Comparison of aberration removal from a real JPEG images from [19] and [15]. We eliminate the aberrations whereas the competitors retain colored edges and cannot restore finer details.

colors and compensating the colored edges. Since the CNN is trained on linear images, prior to restoration we apply an inverse 2.2 gamma curve.

Limitation of the Gaussian model. We showed good performance for eight mid-level camera/lens pairs in our experiments. This guarantees generalization of the Gaussian blur model to that category of photography gear, as claimed by previous art [3, 19, 24]. Yet, this model may be too restrictive in practice, especially for the first-entry lenses for which the lens blur may not be captured by a Gaussian kernel. We show failing examples in the supplementary material.

6 Conclusion

We have proposed a two-stage blind method for removing the lens blur, *i.e.,* its PSF, from a JPEG or raw image. The first module is a blind deblurring technique based on fast 2D Gaussian filter estimation on overlapping patches. We have shown that simple parametric kernels are good approximations of the combination of the monochromatic and longitudinal chromatic aberrations. The second module aligns the red and blue salient edges with the green ones and thus corrects the lateral chromatic aberration. Experiments have shown that the method generalizes to real-world images, even in the presence of the challenging purple fringes. Our approach is also fast, processing a 12 megapixels image in less than 1 second on a GPU, making it suitable for embedding in an ISP pipeline.

Acknowledgements

This work was partly financed by the DGA Astrid Maturation project "SURECAVI" no ANR-21-ASM3-0002, Office of Naval research grant N00014-17-1-2552. This work was performed using HPC resources from GENCI–IDRIS (grant 2022-AD011012453R1).

References

1. Anger, J., Facciolo, G., Delbracio, M.: Blind image deblurring using the ℓ_0 gradient prior. Image Processing Online (IPOL) **9**, 124–142 (2019)
2. Baker, S., Matthews, I.A.: Lucas-Kanade 20 years on: A unifying framework. International Journal on Computer Vision (IJCV) **56**(3), 221–255 (2004)
3. Bauer, M., Volchkov, V., Hirsch, M., Schölkopf, B.: Automatic estimation of modulation transfer functions. In: Proceedings of the International Conference on Computational Photography (ICCP). pp. 1–12 (2018)
4. Boult, T.E., Wolberg, G.: Correcting chromatic aberrations using image warping. In: Proceedings of the conference on Computer Vision and Pattern Recognition (CVPR). pp. 684–687. IEEE (1992)
5. Brauers, J., Seiler, C., Aach, T.: Direct PSF estimation using a random noise target. In: Digital Photography. SPIE Proceedings, vol. 7537, p. 75370. SPIE (2010)
6. Brooks, T., Mildenhall, B., Xue, T., Chen, J., Sharlet, D., Barron, J.T.: Unprocessing images for learned raw denoising. In: Proceedings of the conference on Computer Vision and Pattern Recognition (CVPR). pp. 11036–11045 (2019)
7. Chang, J., Kang, H., Kang, M.G.: Correction of axial and lateral chromatic aberration with false color filtering. IEEE Transactions on Image Processing (TIP) **22**(3), 1186–1198 (2013)
8. Delbracio, M., Garcia-Dorado, I., Choi, S., Kelly, D., Milanfar, P.: Polyblur: Removing mild blur by polynomial reblurring. IEEE Transactions on Computational Imaging (TCI) **7**, 837–848 (2021)
9. Delbracio, M., Musé, P., Almansa, A., Morel, J.: The non-parametric sub-pixel local point spread function estimation is a well posed problem. International Journal on Computer Vision (IJCV) **96**(2), 175–194 (2012)
10. Dube, B., Cicala, R., Closz, A., Rolland, J.: How good is your lens? Assessing performance with MTF full-field displays. Applied Optics **56**(20), 5661–5667 (2017)
11. Eboli, T., Sun, J., Ponce, J.: End-to-end interpretable learning of non-blind image deblurring. In: Proceedings of the European Conference on Computer Vision (ECCV). pp. 314–331 (2020)
12. Foi, A., Trimeche, M., Katkovnik, V., Egiazarian, K.O.: Practical Poissonian-Gaussian noise modeling and fitting for single-image raw-data. IEEE Transactions on Image Processing (TIP) **17**(10), 1737–1754 (2008)
13. Gharbi, M., Chaurasia, G., Paris, S., Durand, F.: Deep joint demosaicking and denoising. ACM Transactions on Graphics (ToG) **35**(6), 191:1–191:12 (2016)
14. Hamilton, J.F., Adams Jr, J.E.: Adaptive color plan interpolation in single sensor color electronic camera (1997), US patent 5629734
15. Heide, F., Rouf, M., Hullin, M.B., Labitzke, B., Heidrich, W., Kolb, A.: High-quality computational imaging through simple lenses. ACM Transactions on Graphics (ToG) **32**(5), 149:1–149:14 (2013)
16. Hirsch, M., Schölkopf, B.: Self-calibration of optical lenses. In: Proceedings of the International Conference on Computer Vision (ICCV). pp. 612–620 (2015)
17. Joshi, N., Szeliski, R., Kriegman, D.J.: PSF estimation using sharp edge prediction. In: Proceedings of the conference on Computer Vision and Patter Recognition (CVPR) (2008)
18. Kang, S.B.: Automatic removal of chromatic aberration from a single image. In: Proceedings of the conference on Computer Vision and Pattern Recognition (CVPR) (2007)

19. Kee, E., Paris, S., Chen, S., Wang, J.: Modeling and removing spatially-varying optical blur. In: Proceedings of the International Conference on Computational Photography (ICCP). pp. 1–8. IEEE Computer Society (2011)
20. Krishnan, D., Fergus, R.: Fast image deconvolution using hyper-Laplacian priors. In: Advances in Neural Information Processing Systems (NeurIPS). pp. 1033–1041 (2009)
21. Leprince, S., Barbot, S., Ayoub, F., Avouac, J.: Automatic and precise orthorectification, coregistration, and subpixel correlation of satellite images, application to ground deformation measurements. IEEE Transactions on Geoscience and Remote Sensing **45**(6), 1529–1558 (2007)
22. Levin, A., Weiss, Y., Durand, F., Freeman, W.T.: Understanding and evaluating blind deconvolution algorithms. In: Proceedings of the conference on Computer Vision and Pattern Recognition (CVPR). pp. 1964–1971. IEEE Computer Society (2009)
23. Li, X., Suo, J., Zhang, W., Yuan, X., Dai, Q.: Universal and flexible optical aberration correction using deep-prior based deconvolution. In: Proceedings of the International Conference on Computer Vision (ICCV). pp. 2593–2601 (2021)
24. Schuler, C.J., Hirsch, M., Harmeling, S., Schölkopf, B.: Non-stationary correction of optical aberrations. In: Proceedings of the International Conference on Computer Vision (ICCV). pp. 659–666 (2011)
25. Schuler, C.J., Hirsch, M., Harmeling, S., Schölkopf, B.: Blind correction of optical aberrations. In: Proceedings of the European Conference on Computer Vision (ECCV). pp. 187–200 (2012)
26. Shih, Y., Guenter, B., Joshi, N.: Image enhancement using calibrated lens simulations. In: Proceedings of the European Conference on Computer Vision (ECCV). pp. 42–56 (2012)
27. Sun, T., Peng, Y., Heidrich, W.: Revisiting cross-channel information transfer for chromatic aberration correction. In: Proceedings of the International Conference on Computer Vision (ICCV). pp. 3268–3276 (2017)
28. Tang, H., Kutulakos, K.N.: What does an aberrated photo tell us about the lens and the scene? In: Proceedings of the International Conference on Computational Photography (ICCP). pp. 1–10 (2013)
29. Tomasi, C., Manduchi, R.: Bilateral filtering for gray and color images. In: Proceedings of the International Conference on Computer Vision (ICCV). pp. 839–846 (1998)
30. Trimeche, M., Paliy, D., Vehvilainen, M., Katkovnik, V.: Multichannel image deblurring of raw color components. In: Computational Imaging. vol. 5674, pp. 169–178. SPIE (2005)
31. Wang, Y., Huang, H., Xu, Q., Liu, J., Liu, Y., Wang, J.: Practical deep raw image denoising on mobile devices. In: Proceedings of the European Conference on Computer Vision (ECCV). pp. 1–16 (2020)
32. Yue, T., Suo, J., Wang, J., Cao, X., Dai, Q.: Blind optical aberration correction by exploring geometric and visual priors. In: Proceedings of the conference on Computer Vision and Pattern Recognition (CVPR). pp. 1684–1692 (2015)
33. Zhang, Z.: A flexible new technique for camera calibration. IEEE Transactions on Pattern Analysis and Machine Intelligence (TPAMI) **22**(11), 1330–1334 (2000)

Fast Two-step Blind Optical Aberration Correction - Supplementary material

We provide additional results and companion analyses to those of the main paper. Section A provides more details on the blind deblurring algorithm, Section B focuses on the proposed CNN and its impact on the restoration pipeline, Section C discusses general implementation details of the method, and Section D shows additional qualitative results for raw images we have taken as well as the JPEG images of [25].

A Deblurring implementation details

A.1 Normalizing function

The normalizing function of Delbracio *et al.* [8] ensures that the images all have ideal latent edges between 0 and 1. We have observed that this is a critical component to make the blur estimation algorithm work. We use the same function as Delbracio *et al.*, defined by

$$n(v_G) = \min\left(\max\left(\frac{v_G - v_G[q]}{v_G[1-q] - v_G[q]}, 0\right), 1\right), \tag{11}$$

where $v_G[q]$ is the q-th quantile of the pixel values in v_G. The quantile value q is set to 0.001 in all the experiments of this presentation.

A.2 Interpolating the angles

We cannot compute the directional image derivative $\nabla_\varphi n(v_G)$ in all the possible angular directions; It would be too slow. We follow [8] and actually compute the derivatives for φ in $\{0, 30, 60, 90, 120, 150, 180\}^\circ$. The then compute the corresponding gradient magnitudes infinite norms

$$\|\nabla_\varphi n(v_G)\|_\infty = \max_x |\nabla_\varphi n(v_G)(x)|,$$

and linearly interpolate these values at every 6° angle, *i.e.,* we predict the infinite norm values for φ in $\{0, 6, 12, \ldots, 174, 180\}^\circ$, before computing the argmax with respect to φ. We have found that in practice this strategy was fast and accurate enough to approximate the real lens blurs.

A.3 Bounding the standard deviation predictions

We predict the parameters of the Gaussian approximation of the blur kernel σ_c (resp. ρ_c) with

$$\sigma_c = \sqrt{\frac{C^2}{\|\nabla_\varphi n(v_c)\|_\infty^2} - \sigma_b^2}, \tag{12}$$

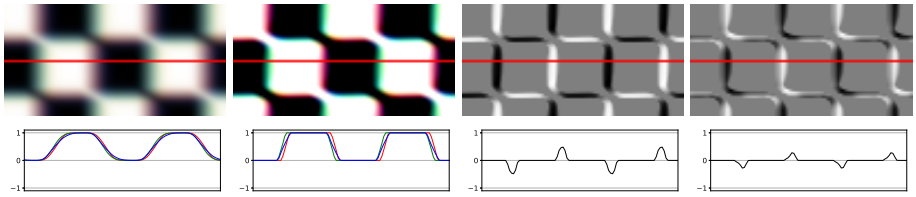

Fig. 9: From left to right: A synthetic aberrated image v, a sharpened version z with noticeable lateral chromatic aberration, the differences $z_R - z_G$ and $z_B - z_G$ showing the support of the colored artifacts. The profile of z shows that the miscorrelation of the three color channels causes the remaining artifacts, detected in the profiles of the images $z_R - z_G$ and $z_B - z_G$.

as in [8]. We however have remarked that when the magnitude of the gradients was to small, *e.g.,* in textured areas like a tree seen from afar, this equation was predicting a very large blur, even with the normalization function. As discussed in Section C, increasing the patch size may help. To limit this problem Delbracio *et al.* proposed a clipping strategy. However, in this work we use the following conservative strategy

$$\sigma_c^\star = \begin{cases} 0.2 \text{ if } \sigma_c > 4 \text{ or } V(n(v_c)) < \tau, \\ \sigma_c \text{ otherwise,} \end{cases} \tag{13}$$

where V is the variance operator and the threshold τ is set to 0.09. This strategy leads to a filter similar to a Dirac impulse, preventing deblurring artifacts in case of ill-blur prediction or "flat" patch, *e.g.,* a patch with only the sky. The same technique is also applied to ρ_c.

B CNN details

B.1 Motivation for the loss design

As we said in the main paper, we follow Chang *et al.* [7] and leverage the property that the green/red and green/blue image residuals are good features to detect chromatic aberrations in a photograph. Figure 9 shows an example for a checker grid image. Bumps on the profiles of the residuals indicate the presence of colored edges, most likely aberrations. When training a CNN, we minimize these quantities so the bumps are as small as possible.

B.2 Architecture

We detail the architecture of ϕ for predicting the colored residual in Table 1. We call C a convolutional layer, R a ReLU activation, B a batch normalization module and "Add d" a block that adds to the current feature map the output

Tag	1	2	3	4	5	6	7	8	9	10	11
Layer	CBR	CBR	CBR	CBR	CBR	Add 3	CBR	Add 2	CBR	Add 1	C
Dim	16×2	32×16	64×32	64×64	64×64	-	32×64	-	16×32	-	1×16

Table 1: Detail of the architecture of ϕ in the main paper for edge correction.

of layer d. All the convolutions have 3×3 filters and the dimensions are given with the format "output/input" channels.

Note that the input channel width is set to 2 since it combines the green and either the red or the blue channel, and returns a residual for the red or the blue channel.

B.3 Training data generation

We detail in this section the training data for learning the optimal parameter ν of the CNN. The generation may be divided into four main stages, resulting in a deblurred but with colored-edges image and its sharp counterpart:

1. Unprocessing a JPEG image with the pipeline of Brooks *et al.* [6]. We invert tone-mapping with their proposed inverse S-curve function and gamma compression with the exponent 2.2. This yields a synthetic RGB image with linear values with respect to the electron counts;
2. Blurring and adding noise to the raw image. The simulated blurs are Gaussian filters with standard deviation values ρ_c and σ_c ($c = R, G, B$) in [0.2, 4] and sub-pixel horizontal and vertical translations in [-4,4]. The blurry and noisy patch is finally mosaicked with the RGGB Bayer pattern;
3. Denoising and demosaicking the synthetic raw image to mimic the two first stages of an image editing software. Because of speed for generating the training data, we use the bilateral filter [29] for denoising and the Hamilton-Adams algorithm [14] for demosaicking;
4. Deblurring the raw patch with the blind deblurring technique detailed in Section 4.1: From the denoised and demosaicked patch, we first predict the orientation θ and the color-dependent standard deviation values σ_c and ρ_c, and second we remove the blur with the approximate inverse filter defined by the polynomial p.

In this work we used the bilateral filter of for denoising and the Hamilton-Adams interpolator for fast demosaicking. We used these algorithms since they are fast but training may be indeed enhanced with CNN-based algorithms, *e.g.,* the blind denoiser of Wang *et al.* [31] and the demosaicking module of Gharbi *et al.* [13].

B.4 Choice of the loss

We have shown in the main paper that the proposed loss in Eq. (8), built over red/green and blue/green residuals is pivotal to achieve colored edge correction.

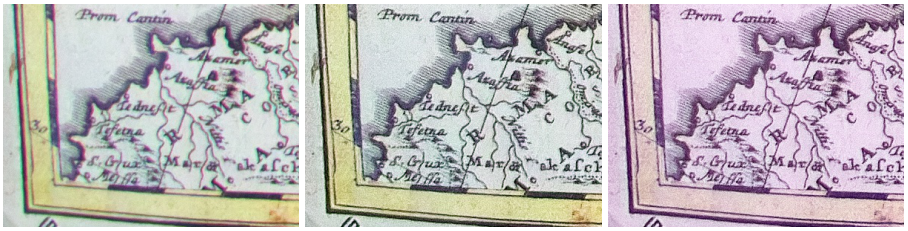

(a) Aberrated. (b) Loss in Eq. (8). (c) Gradient variant.

Fig. 10: Comparison of the color biases introduces by training loss, whether we evaluate the difference of the pixel values, *i.e.,* $\|(\widehat{u}_c - z_G) - (u_c - u_G)\|_1$, or the gradient values, *i.e.,* $\|\nabla(\widehat{u}_c - z_G) - \nabla(u_c - u_G)\|_1$, as advised by the prior of Heide *et al.* [15]. The loss on pixel value residuals retains the same exposure and color palette as in the original aberrated image, whereas the one on the gradients introduces a pinkish bias. Note that both versions actually compensate the colored edges.

Fig. 11: The ten 6000×4000 images (24 megapixels) we use for the quantitative analysis of the edge correction algorithm. Each image features salient edges, prone to lateral chromatic aberrations. The reader is invited to zoom in on a computer screen.

However the prior of Heide *et al.* [15] in Eq. (13) compares the gradients of the color channel. Training the CNN ϕ with a loss minimizing the gradients of the residuals instead, and reminiscent of Eq. (13), is sub-optimal since there is no reference to the pixel, and leads to a wrong average color in the image. Thus, the residual-based training loss prevents these issues, leverages the property of the lateral chromatic aberrations detailed in [7], and leads to solutions minimizing the prior of Heide *et al.* at the same time. Figure 10 shows an example of this phenomenon. We have noted that the combination of the loss on the pixel values in Eq. (8) and on the gradients of the color residuals was leading to marginal gains compared to that only minimizing the pixel values of the colored residuals, validating Eq. (8).

(a) Original (b) Size 100 (c) Size 200 (d) Size 400 (e) Size 800

Fig. 12: Qualitative comparison of the impact of the patch size on the peformance of the blind deblurring module on a real aberrated image. From left to right: the aberrated image and restored versions where the patch size is respectively 100, 200, 400 and 800. For patch sizes of 400 or 800, the image is actually deblurred. Under, the image is either blurry or contains artifacts. Note the presence of colored edges, *e.g.,* next ot the electrical cable, since we show images solely deblurred, prior to any evaluation with the CNN ϕ. The reader is invited to zoom in on a computer screen.

C Whole pipeline details

C.1 Test images

We show in Figure 11 the ten images we use for evaluating the edge correction algorithms in the experiment section of the main paper. The images where taken with the Sony α6000 camera, the Sony FE 35mm $f/1.8$ lens at maximal aperture and the Sigma 18-50mm $f/2.8$ DC DN lens at maximal aperture and shortest focal length.

C.2 Patch size

Setting the size of the patches is critical for the success of the blur estimation technique of Delbracio *et al.* [8] in the context of spatially-varying blurs. Indeed, this method is based on the presence of salient edges and may fail if there are too few edges on the patch support, *e.g.,* for too small patches. We show in Fig. 12 the comparison of an image crop for images deblurred with different patch sizes, ranging from 100 to 800 pixels. We restore non-overlapping patches to visualize what the deblurring exactly restores on each patch. In this figure one can see that for the patch size set to 100 the image looks almost like the original one. For the patch size set to 200, noticeable deconvolution artifacts can be seen next to the leaves. For the patch size set to 400 and 800, the restored results are plausible.

The result for the patch size of 200 may be explained by the fact that, to work well the blur estimation method needs edges with important contrast. However, in textured regions with only moderate gradients, the affine rule may predict

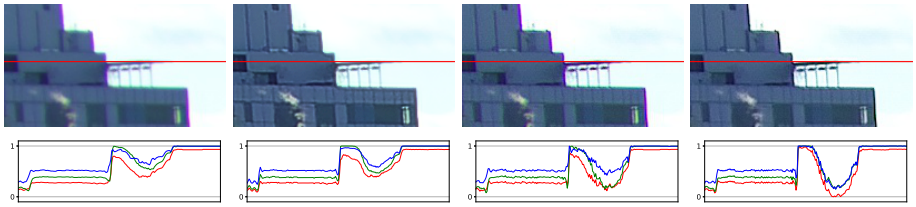

Fig. 13: Comparison of purple fringe removal from a real raw image. From left to right: The blurry image, the version restored with DxO PhotoLab 5 (non-blind), and the images only deblurred and deblurred+corrected by our model (blind).

a larger standard deviation value than the real one, resulting in a too large deconvolution filter and thus artifacts in the final image. A Weakness of this affine rule is thus such regions, and a simple way to prevent these artifacts is selecting larger patches to favor the presence of more contrasted edges. In this presentation, we set the patch size to 400, which is valid for most images we have tested our approach on.

C.3 Saturation

The combination of optical chromatic aberrations and saturation is called by photographers "purple fringes", an artifact challenging to remove. Yet, our technique successfully compensates these fringes as shown in Fig. 13. However, despite good performance on real images our approach cannot remove all the purple fringes, and leaves a thin dark line next to saturated areas. As previously noted, the performance of our method is closely related to that of the blur estimation stage, which makes the assumption that there is at least one strong edge in the patch, and thus may fail in textured regions.

D Additional images

D.1 Raw images

To qualitatively validate our approach, we have taken several photographs with a Sony α6000 camera, and combined with the Sony FE 35mm $f/1,8$ and the Sigma 18-50mm $f/2.8$ DC DN lenses. We compare our approach to the commercial software DxO PhotoLab 5, whose catalog contains the profile of the Sony lens, but not that of the Sigma one recently released in October 2021. PhotoLab thus runs in a non-blind setting for the 35mm lens, and should achieve the best result over our technique, whereas it runs in a blind setting for the Sigma lens. The images dubbed "culture", "map" and "tree" are shown in Figure 14, and magnified crops are shown in Figures 15, 16 and 17. The tree example in Figure 17 illustrates in particular the robustness of our method to "purple fringes", *i.e.,* the combination of optical aberrations and saturation.

(a) Culture (Sony lens). (b) Map (Sigma lens). (c) Tree (Sony lens).

Fig. 14: The additional images for qualitative evaluation. The images are denoised and demosaicked with DxO PhotoLab 5.

D.2 JPEG images

We also compare the restoration of JPEG images, with the methods of [24], [25] and [27] when the images are available. Our method achieves overall the best results. The images dubbed "facade" and "bridge" are shown in Figure 18, and magnified crops are shown in Figures 19 and 20.

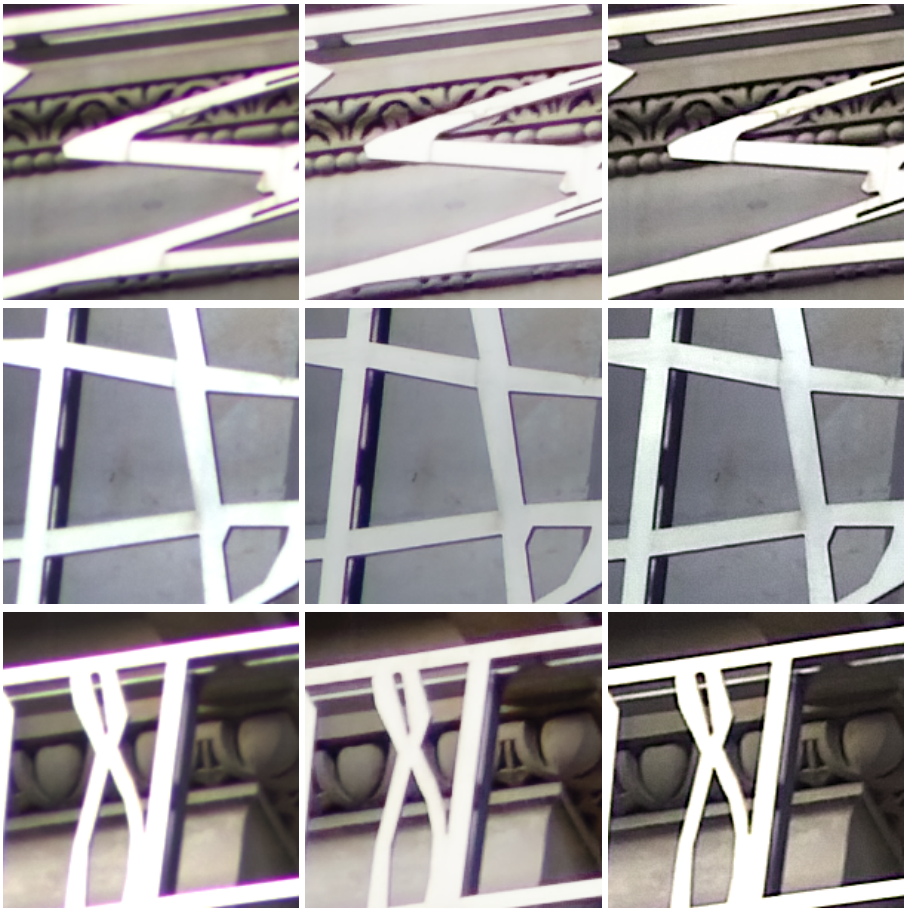

(a) Blurry. (b) DxO. (c) Ours.

Fig. 15: Crops for the "map" image taken with the Sony FE 35mm $f/1.8$ lens. From left to right: the original blurry image, the optical aberration correction of DxO PhotoLab (non-blind setting), and ours.

(a) Blurry. (b) DxO. (c) Ours.

Fig. 16: Crops for the "map" image taken with the Sigma 18-50mm $f/2.8$ DC DN lens. From left to right: the original blurry image, the optical aberration correction of DxO PhotoLab (blind setting), and ours.

(a) Blurry. (b) DxO. (c) Ours.

Fig. 17: Crops for the "tree" image taken with the Sony FE 35mm $f/1.8$ lens. From left to right: the original blurry image, the optical aberration correction of DxO PhotoLab (non-blind setting), and ours.

(a) Facade (b) Bridge

Fig. 18: The additional JPEG images from [25] for qualitative evaluation.

(a) Blurry. (b) [24]. (c) [25]. (d) [27]. (e) Ours.

Fig. 19: Crops for the "Facade" image from [25]. From left to right: the original blurry image, the non-blind result of Schuler *et al.* [24], the blind result of Schuler *et al.* [25], the blind result of Sun *et al.* [27], and ours.

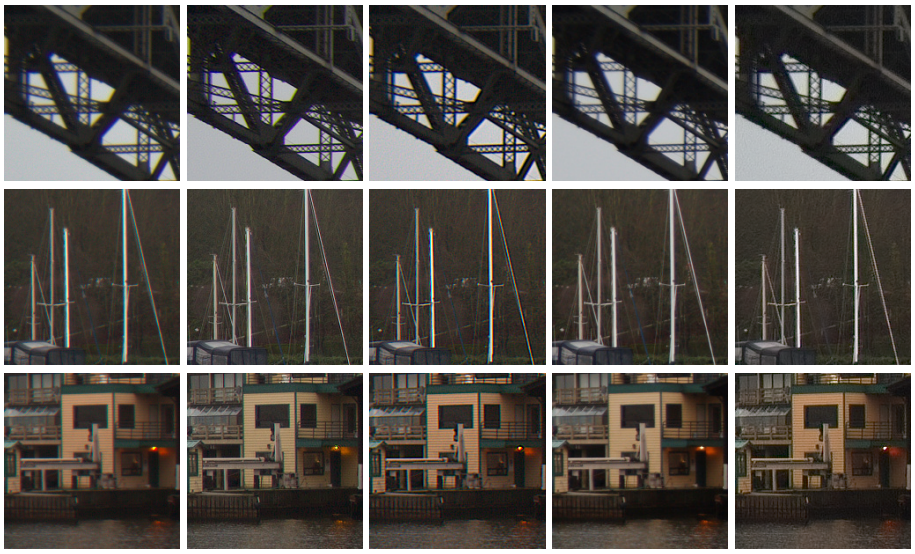

(a) Blurry. (b) [19]. (c) [25]. (d) DxO ([25]). (e) Ours.

Fig. 20: Crops for the "Bridge" image from [25]. From left to right: the original blurry image, the non-blind result of Kee *et al.* [24], the blind result of Schuler *et al.* [25], the blind result of DxO (runned by Schuler *et al.* [25]), and ours.